# Room-temperature detection of a single 19nm super-paramagnetic nanoparticle with an imaging magnetometer

Michael Gould, Russell J. Barbour, Nicole Thomas, Hamed Arami, Kannan M. Krishnan, and Kai-Mei C. Fu

Citation: Applied Physics Letters **105**, 072406 (2014); doi: 10.1063/1.4893602
View online: http://dx.doi.org/10.1063/1.4893602
View Table of Contents: http://scitation.aip.org/content/aip/journal/apl/105/7?ver=pdfcov
Published by the AIP Publishing

# Room-temperature detection of a single 19 nm super-paramagnetic nanoparticle with an imaging magnetometer

Michael Gould,[1,a)] Russell J. Barbour,[2] Nicole Thomas,[1] Hamed Arami,[3] Kannan M. Krishnan,[3] and Kai-Mei C. Fu[1,2]
[1]*Department of Electrical Engineering, University of Washington, Seattle, Washington 98195-2500, USA*
[2]*Department of Physics, University of Washington, Seattle, Washington 98195-1560, USA*
[3]*Department of Material Science and Engineering, University of Washington, Seattle, Washington 98195-2120, USA*

(Received 3 March 2014; accepted 9 August 2014; published online 19 August 2014)

We demonstrate room temperature detection of isolated single 19 nm super-paramagnetic nanoparticles (SPNs) with a wide-field optical microscope platform suitable for biological integration. The particles are made of magnetite ($Fe_3O_4$) and are thus non-toxic and biocompatible. Detection is accomplished via optically detected magnetic resonance imaging using nitrogen-vacancy defect centers in diamond, resulting in a DC magnetic field detection limit of 2.4 $\mu$T. This marks a large step forward in the detection of SPNs, and we expect that it will allow for the development of magnetic-field-based biosensors capable of detecting a single molecular binding event. © *2014 AIP Publishing LLC*. [http://dx.doi.org/10.1063/1.4893602]

Super-paramagnetic nanoparticles (SPNs) are particles made of ferromagnetic material which, due to their small size, exhibit paramagnetic behavior with magnetic susceptibilities orders of magnitude larger than typical paramagnetic materials.[1] Magnetite ($Fe_3O_4$) SPNs can be readily functionalized for specific binding to a wide variety of molecules,[2–6] and are thus particularly useful for biological detection and imaging applications.[7–10] However, the detection of *single* SPNs in biologically compatible systems has remained an unsolved problem. Applications that would benefit greatly from this capability include highly sensitive assays for cancer,[11,12] HIV,[13] and non-acute-coronary-syndrome cardiac conditions.[14] In particular, digital immuno-assays rely on the detection of single bio-molecules to achieve ultra-high detection sensitivities.[15,16] In this work, we experimentally realize a room temperature platform capable of detecting single 19 nm diameter magnetite SPNs using wide-field optical imaging.

SPNs offer several advantages over conventional fluorescent tags. SPNs are detected magnetically, and thus the biological system under investigation can theoretically be completely isolated from optical fields, reducing undesired optical and thermal interactions. Furthermore, while the majority of biological samples exhibit fluorescence, they typically do not exhibit magnetism, potentially allowing for higher background contrast in SPN-based sensing schemes. Finally, SPN tags may allow for spatial manipulation of tagged molecules and the removal of unbound tags through the application of a magnetic field gradient.[17,18]

Several SPN detection schemes have been demonstrated, such as giant magneto-resistive (GMR) sensors,[19,20] magnetic force microscopy (MFM),[21] superconducting quantum interference devices (SQUIDs),[22] micro-Hall sensors,[23,24] and magnetic tunnel junctions (MTJs).[25] Of the methods listed above, detection of single magnetic particles with diameters under 1 $\mu$m has only been demonstrated with SQUIDs and MFM. SQUIDs require operation at cryogenic temperatures while MFM makes use of a nano-mechanical scanning probe in contact with the sensing surface. Thus, neither of these platforms is ideal for biological integration.

Our platform uses negatively charged nitrogen-vacancy (NV) centers in diamond to detect the magnetic field from SPNs. NVs are point defects in the diamond crystal lattice consisting of a substitutional nitrogen atom and a vacancy occupying nearest-neighbor lattice sites. The long electron spin coherence times of the NV ground state (up to 1.8 ms at room temperature),[26,27] combined with spin-dependent optical transitions, make NV centers attractive for highly sensitive magnetometry applications.[28,29] For example, single NV centers have been used to detect single nuclear spins within the diamond lattice.[30–32] Ensembles of NVs can also be used for two-dimensional magnetic field imaging over larger regions, but with reduced sensitivity.[33–35] Using ensemble-based sensing, we are able to image disturbances in a uniform applied magnetic field due to the presence of SPNs.

NV centers can be viewed as a localized 2-electron system with the energy-level diagram shown in Figure 1(a). The ground state of the system is a spin-triplet, for which the $m_s = \pm 1$ spin states are degenerate under zero applied magnetic field, and split from the $m_s = 0$ spin state by an energy $E_{ss}$ due to spin-spin interactions.[36,37] Under an applied DC magnetic field, the Zeeman effect causes the $m_s = \pm 1$ ground states to split,[34,35] with respective energy shifts of $\Delta E = \pm g\mu_B \vec{B} \cdot \hat{z}$, where $g$ is the electron g-factor, $\mu_B$ is the Bohr magneton, $\vec{B}$ is the applied DC magnetic field, and $\hat{z}$ is a unit vector aligned with the NV symmetry axis. Thus by detecting $\Delta$E, the component of the applied field aligned with the NV axis can be determined.

Optical detection of $\Delta$E is made possible by the presence of a decay path from the $m_s = \pm 1$ excited states, through two singlet states, to the $m_s = 0$ ground state.[37,38] This causes the $m_s = \pm 1$ states to emit less photoluminescence (PL) relative to the $m_s = 0$ state, and also allows for

a)Author to whom correspondence should be addressed. Electronic mail: mike.gould23@gmail.com.

 

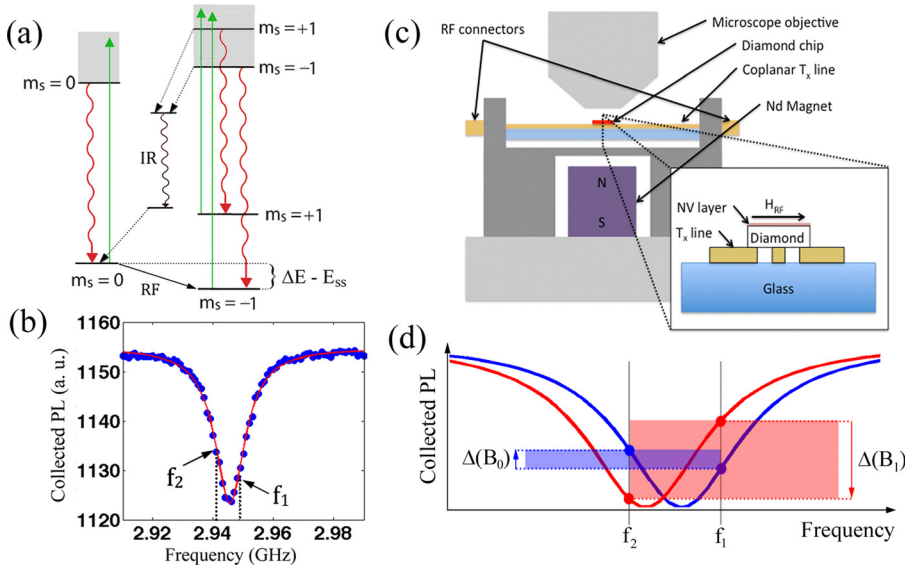


FIG. 1. (a) Energy level diagram for an NV center. Green arrows represent 532 nm excitation and red arrows represent radiative decay in the collection band. Note that only zero-phonon decay is depicted and energy level spacings are not drawn to scale. (b) Experimental ODMR curve taken with a ~200 mT magnetic field applied at the sensing surface. The frequency bias points for imaging are indicated as $f_1$ and $f_2$. Blue circles are experimental data points and the solid red line is a Lorentzian fit. (c) Schematic of setup below microscope objective showing the arrangement of the RF transmission line ($T_x$ line), Nd magnet, and diamond chip. Inset shows a zoomed-in cut through the diamond chip and $T_x$ line. (d) Diagram of difference detection scheme, with the blue curve representing an ODMR curve under the background field and the red curve representing a shift in resonance due to a change in magnetic field. The colored arrows and rectangles represent the difference signal in each case.

optical pumping to the $m_s = 0$ spin state. Under constant optical excitation, an RF magnetic field resonant with a ground state spin transition can be used to transfer population to a $m_s = \pm 1$ spin state, resulting in a decrease in detected PL. An example of an optically detected magnetic resonance (ODMR) curve is shown in Figure 1(b), in which collected PL intensity is measured as a function of RF. A 3% dip is observed at 2.945 GHz, corresponding to the $m_s = 0$ to $m_s = -1$ spin transition for NV centers aligned to the applied field.

In this work, we perform imaging ODMR measurements on a 200 nm-thick, high-density sheet of NV centers near the {111} surface of a diamond chip.[39] As depicted in Figure 1(c), the sensing chip sits on a co-planar transmission line used to apply an RF magnetic field in the plane of the chip surface. A neodymium (Nd) magnet sits below, applying a DC magnetic field of approximately 200 mT at the surface, aligned to the surface normal and thus to one of the four distinguishable ⟨111⟩ NV orientations. The chip is imaged using standard wide-field fluorescence microscopy, with a 10 $\mu$m diameter excitation area and a resolution of approximately 500 nm.[39]

Using this setup, the spatial distribution of the component of the magnetic field normal to the chip surface is imaged. We use a simple difference imaging scheme utilizing only NVs aligned with the applied DC field. Field images are obtained as a difference of PL images taken with the applied RF magnetic field set to two different frequencies. As illustrated in Figure 1(d), resonance shifts due to changes in magnetic field result in changes in the PL intensity difference between the two RF states. The frequencies are chosen to be just below the steepest parts of the ODMR curve on either side of the resonance ($f_1$ and $f_2$ in Figures 1(b) and 1(d)), maintaining a high small-field sensitivity while increasing the signal from the high field in proximity to SPNs.

In order to characterize the system's SPN detection capability, magnetite SPNs with a median core size of $16.9 \pm 0.46$ nm and a standard deviation of the log-normal distribution of $0.249 \pm 0.036$ were deposited on the sensing surface in isolated single particles and small groups. The SPNs were synthesized according to a previously reported method,[39–43] and exhibited magnetic saturation for applied fields greater than ~50 mT. Particle distributions were obtained by drying colloidal suspensions on a lithographically defined pattern on the sensor surface, resulting in a grid pattern with small groups of particles at each grid point. Figure 2(a) shows a scanning electron microscope (SEM) image of a resulting pattern of particle groups.[39]

Figure 2(b) shows a magneto-optical image of the area shown in Figure 2(a), obtained using the difference-imaging scheme described above. The total exposure time for each RF field state was 10 s, with no improvement in the signal-to-noise ratio (SNR)[39] observed for increased integration time. Single particles, indicated by black arrows, are visible as dark spots in the image. The upper left grid spot, indicated with a white arrow, contains no SPNs and there is correspondingly no detected signal. Zoomed-in SEM images of both single-particle grid spots, as well as the empty grid spot, are shown in Figures 2(d)–2(f). Two grid spots containing two particles are also shown in Figures 2(g) and 2(h). Horizontal line cuts through the particles show diameters close to 19 nm, confirming their single-particle nature. A horizontal line cut through the center of the image is also included in Figure 2(f) for comparison.

Including a second nearby imaging area,[39] a total of 18 grid spots containing between 0 and 5 particles were imaged. The detection of single particles and small groups is summarized in Figure 3, where the signal-to-noise ratio for each group is plotted as a function of particle count.[39] Importantly, all groups and single particles were detected with SNR values

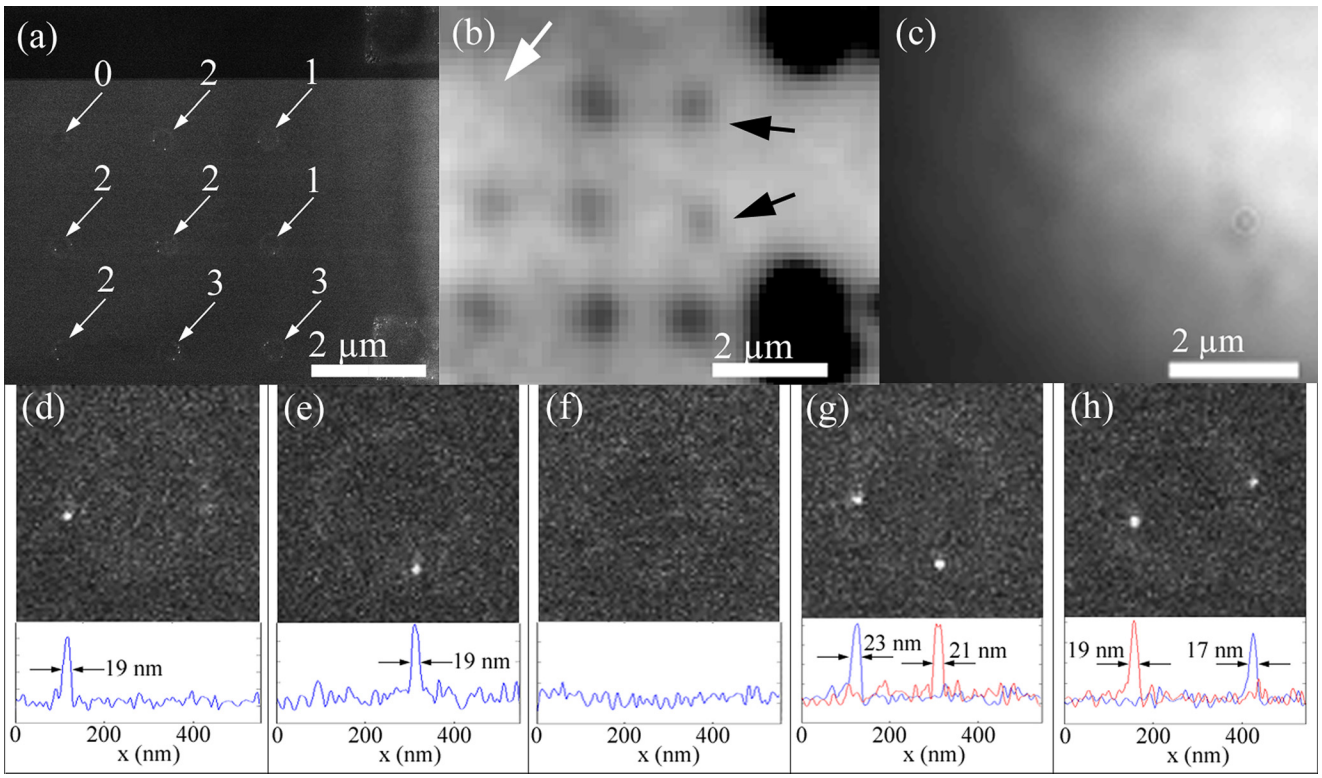


FIG. 2. (a) SEM image of small groups of SPNs arranged in a grid pattern, with particle number noted for each group. (b) A magneto-optical image of area shown in (a). (c) PL image of area shown in (a). (d) SEM image of single particle in upper-right grid spot in (a), with horizontal cut data taken through the particle. (e) SEM image of single particle in center-right grid spot in (a), with horizontal cut data taken through the particle. (f) SEM image of empty grid spot (upper-left) in (a), with horizontal cut data taken through center of image. (g) SEM image of upper-middle grid spot in (a) containing two particles, with horizontal cut data taken through both particles. (h) SEM image of center-left grid spot in (a) containing two particles, with horizontal cut data taken through both particles.

greater than 1.5, indicating that only a single particle is required within the field of view of the microscope for positive detection. For many applications, such as those requiring imaging of isolated single SPN-tagged biomolecules, this is an important capability. We note, however, that due to variations in signal between different groups of the same size, the system cannot currently be used for exact particle counting. The data suggest that particle number can at best be estimated to within $\pm 1$ particle for group sizes $<5$. The dominant source of variation in signal strength for a given group size is likely variation in particle size. In fact, the measured particle size variation[39] corresponds to a variation in magnetic moment between a factor of 3.8 and 6.5. Neither a variation in the easy-axis orientation of the SPNs, nor a variation in NV-particle distance are expected to be contributing significantly to the signal variation.[39]

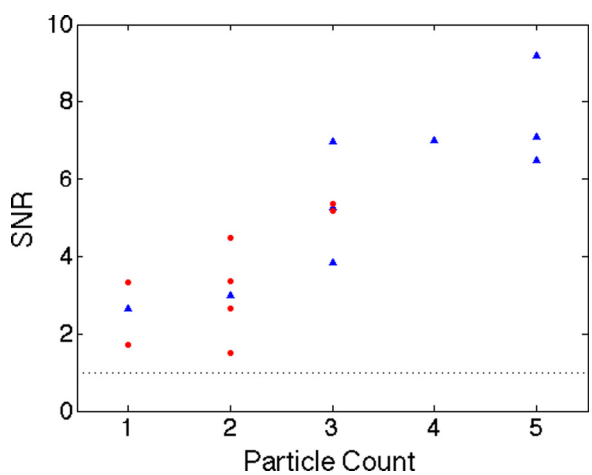


FIG. 3. Plot of SNR as a function of particle count for all 17 non-zero groups in both imaging areas. Red circles correspond to groups in the first imaging area (Figure 2), while blue triangles represent groups in the second area. Dashed line is noise floor (SNR = 1).

We define the magnetic field limit-of-detection (LOD) as the magnetic field required to cause a change in pixel value equivalent to the 3-sigma noise in a control area. The control area is chosen to be a $7 \times 7$ pixel square in close proximity to the wells, and the measured noise corresponds to an LOD of 2.4 $\mu$T. This is in reasonable agreement with the expected value of 3.8 $\mu$T, based on experimental ODMR spectra from the chip, the optical resolution of the system and the exposure time used.[39] However, as stated above, we observe a lack of improvement in the LOD with longer integration, suggesting that field detection is limited by some source of time-invariant spatial fluctuation in the ODMR signal.

By using bias points on either side of the resonance, our detection scheme mitigates the effect of fluctuations that are symmetric about the resonance such as variations in the depth and width of the ODMR curve. However, the system remains susceptible to variations that are anti-symmetric about the resonance. For example, strain variation within the chip may cause local shifts in the frequency of the spin transitions.[36,37,44] We expect to be able to mitigate this effect and further improve the limit-of-detection of the system by carefully measuring the ODMR spectrum of each pixel in the

imaging area prior to any sensing experiments, allowing for subsequent computational image correction. Other possible sources of spatial noise are systematic spatial and thermal shifts between RF states, which could be reduced by mechanical and thermal isolation of RF components from the rest of the system. Additional paths to improved detection include using samples with longer spin-dephasing times, the use of thinner NV layers obtained using $He^+$ implantation[45,46] or by direct incorporation of NV centers during epitaxial diamond growth,[47] and improved PL collection efficiency.[48] Ultimate sensitivity will result from an optimized NV density balancing spin coherence time and PL brightness,[28] an NV layer thickness optimized for the diameter and magnetic moment of the particles to be detected, and collection efficiency into the first objective much higher than the estimated 3% obtained on the current setup.

In summary, we have demonstrated room temperature detection of single 19 nm magnetite SPNs using wide-field optical microscopy. The significant advantage of this system over others capable of single SPN detection is its relative simplicity; detection does not require cryogenic temperatures or nano-mechanical components, leaving it open to integration with biological and other nano-scale surface-based experiments. This marks a significant step forward in the detection of SPNs, and we expect that it will allow for the development of bio-sensors capable of detecting a single molecular surface binding event. Continued improvements in sensitivity will allow for further applications in biological detection and imaging, as well as broader applications in the study of nano-scale magnetic systems.

The authors would like to acknowledge support from the Washington Nanofabrication Facility, and would like to thank Richard Bojko for electron beam lithography support, R. M. Ferguson for providing nanoparticle samples, Todd Karin for help with SEM image processing, and James Lai for helpful discussion regarding applications. Financial support for this work was provided by the University of Washington Royalty Research Fund award A79342. M. Gould received financial support from the Natural Science and Engineering Research Council of Canada through a Post-Graduate Scholarship.

[1]C. Bean and J. Livingston, J. Appl. Phys. **30**, S120 (1959).
[2]H. Lu, G. Yi, S. Zhao, D. Chen, L.-H. Guo, and J. Cheng, J. Mater. Chem. **14**, 1336 (2004).
[3]O. Veiseh, C. Sun, C. Fang, N. Bhattarai, J. Gunn, F. Kievit, K. Du, B. Pullar, D. Lee, R. G. Ellenbogen *et al.*, Cancer Res. **69**, 6200 (2009).
[4]C. Sun, K. Du, C. Fang, N. Bhattarai, O. Veiseh, F. Kievit, Z. Stephen, D. Lee, R. G. Ellenbogen, B. Ratner *et al.*, ACS Nano **4**, 2402 (2010).
[5]Y. Jin, C. Jia, S.-W. Huang, M. O'Donnell, and X. Gao, Nat. Commun. **1**, article number 41 (2010).
[6]J. Gao, H. Gu, and B. Xu, Acc. Chem. Res. **42**, 1097 (2009).
[7]M. Brzeska, M. Panhorst, P. B. Kamp, J. Schotter, G. Reiss, A. Pühler, A. Becker, and H. Brückl, J. Biotechnol. **112**, 25 (2004).
[8]Y. R. Chemla, H. L. Grossman, Y. Poon, R. McDermott, R. Stevens, M. D. Alper, and J. Clarke, Proc. Natl. Acad. Sci. U. S. A. **97**, 14268 (2000).
[9]J. B. Haun, T.-J. Yoon, H. Lee, and R. Weissleder, Wiley Interdiscip. Rev.: Nanomed. Nanobiotechnol. **2**, 291 (2010).
[10]K. Krishnan, IEEE Trans. Magn. **46**, 2523 (2010).
[11]J. D. Wulfkuhle, L. A. Liotta, and E. F. Petricoin, Nat. Rev. Cancer **3**, 267 (2003).
[12]X. Liu, Q. Dai, L. Austin, J. Coutts, G. Knowles, J. Zou, H. Chen, and Q. Huo, J. Am. Chem. Soc. **130**, 2780 (2008).
[13]M. Miedouge, M. Grèze, A. Bailly, and J. Izopet, J. Clin. Virol. **50**, 57 (2011).
[14]J. A. de Lemos, JAMA **309**, 2262 (2013).
[15]D. H. Wilson, D. W. Hanlon, G. K. Provuncher, L. Chang, L. Song, P. P. Patel, E. P. Ferrell, H. Lepor, A. W. Partin, D. W. Chan *et al.*, Clin. Chem. **57**, 1712 (2011).
[16]L. Chang, L. Song, D. R. Fournier, C. W. Kan, P. P. Patel, E. P. Ferrell, B. A. Pink, K. A. Minnehan, D. W. Hanlon, D. C. Duffy *et al.*, J. Virol. Methods **188**, 153 (2013).
[17]K. S. Kim and J.-K. Park, Lab Chip **5**, 657 (2005).
[18]C. Hoffmann, E. Mazari, S. Lallet, R. Le Borgne, V. Marchi, C. Gosse, and Z. Gueroui, Nat. Nanotechnol. **8**, 199 (2013).
[19]G. Li, V. Joshi, R. L. White, S. X. Wang, J. T. Kemp, C. Webb, R. W. Davis, and S. Sun, J. Appl. Phys. **93**, 7557 (2003).
[20]R. S. Gaster, L. Xu, S.-J. Han, R. J. Wilson, D. A. Hall, S. J. Osterfeld, H. Yu, and S. X. Wang, Nat. Nanotechnol. **6**, 314 (2011).
[21]T. Nocera, J. Chen, C. Murray, and G. Agarwal, Nanotechnology **23**, 495704 (2012).
[22]C. Thirion, W. Wernsdorfer, and D. Mailly, Nat. Mater. **2**, 524 (2003).
[23]M. Gabureac, L. Bernau, G. Boero, and I. Utke, IEEE Trans. Nanotechnol. **12**, 668 (2013).
[24]G. Mihajlovic and P. Xiong, Appl. Phys. Lett. **87**, 112502 (2005).
[25]W. Shen, X. Liu, D. Mazumdar, and G. Xiao, Appl. Phys. Lett. **86**, 253901 (2005).
[26]N. Bar-Gill, L. M. Pham, A. Jarmola, D. Budker, and R. L. Walsworth, Nat. Commun. **4**, 1743 (2013).
[27]G. Balasubramanian, P. Neumann, D. Twitchen, M. Markham, R. Kolesov, N. Mizuochi, J. Isoya, J. Achard, J. Beck, J. Tissler *et al.*, Nat. Mater. **8**, 383 (2009).
[28]J. Taylor, P. Cappellaro, and L. Childress, Nat. Phys. **4**, 810 (2008).
[29]C. L. Degen, Appl. Phys. Lett. **92**, 243111 (2008).
[30]N. Zhao, J. Honert, B. Schmid, and M. Klas, Nat. Nanotechnol. **7**, 657 (2012).
[31]P. Neumann, J. Beck, M. Steiner, F. Rempp, H. Fedder, P. R. Hemmer, J. Wrachtrup, and F. Jelezko, Science **329**, 542 (2010).
[32]L. Robledo, L. Childress, H. Bernien, B. Hensen, P. F. A. Alkemade, and R. Hanson, Nature **477**, 574 (2011).
[33]S. Steinert, F. Dolde, P. Neumann, A. Aird, B. Naydenov, G. Balasubramanian, F. Jelezko, and J. Wrachtrup, Rev. Sci. Instrum. **81**, 043705 (2010).
[34]L. Pham and D. Le Sage, New J. Phys. **13**, 045021 (2011).
[35]B. J. Maertz, A. P. Wijnheijmer, G. D. Fuchs, M. E. Nowakowski, and D. D. Awschalom, Appl. Phys. Lett. **96**, 092504 (2010).
[36]N. Manson, J. Harrison, and M. Sellars, Phys. Rev. B **74**, 104303 (2006).
[37]A. Lenef and S. Rand, Phys. Rev. B **53**, 13441 (1996).
[38]V. Acosta, A. Jarmola, E. Bauch, and D. Budker, Phys. Rev. B **82**, 201202 (2010).
[39]See supplementary material at http://dx.doi.org/10.1063/1.4893602 for a more complete description of the experimental optical setup and details concerning chip fabrication, SPN synthesis, characterization and deposition details, noise and LOD definitions and considerations, and a SEM image of the second imaging area.
[40]H. Arami and R. Ferguson, Med. Phys. **40**, 071904 (2013).
[41]R. M. Ferguson, A. P. Khandhar, and K. M. Krishnan, J. Appl. Phys. **111**, 07B318 (2012).
[42]A. P. Khandhar, R. M. Ferguson, J. A. Simon, and K. M. Krishnan, J. Biomed. Mater. Res., Part A **100**, 728 (2012).
[43]A. P. Khandhar, R. M. Ferguson, H. Arami, and K. M. Krishnan, Biomaterials **34**, 3837 (2013).
[44]P. Olivero, F. Bosia, B. A. Fairchild, B. C. Gibson, A. D. Greentree, P. Spizzirri, and S. Prawer, New J. Phys. **15**, 043027 (2013).
[45]Z. Huang, W.-D. Li, C. Santori, V. M. Acosta, A. Faraon, T. Ishikawa, W. Wu, D. Winston, R. S. Williams, and R. G. Beausoleil, Appl. Phys. Lett. **103**, 081906 (2013).
[46]D. McCloskey, D. Fox, N. O'Hara, V. Usov, D. Scanlan, N. McEvoy, G. S. Duesberg, G. L. W. Cross, H. Z. Zhang, and J. F. Donegan, Appl. Phys. Lett. **104**, 031109 (2014).
[47]T. Ishikawa, K.-M. C. Fu, C. Santori, V. M. Acosta, R. G. Beausoleil, H. Watanabe, S. Shikata, and K. M. Itoh, Nano Lett. **12**, 2083 (2012).
[48]T. K. Yeung, D. Le Sage, L. M. Pham, P. L. Stanwix, and R. L. Walsworth, Appl. Phys. Lett. **100**, 251111 (2012).